ACS APPLIED MATERIALS & INTERFACES

Research Article

www.acsami.org

Organic Nanocomposite Structure Tailored by Controlling Droplet Coalescence during Inkjet Printing

Andrew C. Ihnen,[†] Anne M. Petrock,[‡] Tsengming Chou,[†] Brian E. Fuchs,[‡] and Woo Y. Lee*,[†]

[†]Department of Chemical Engineering and Materials Science, Stevens Institute of Technology, Hoboken, New Jersey 07030, United States

[‡]U.S. Army – Armament Research, Development and Engineering Center, Picatinny Arsenal, New Jersey 07806, United States

ABSTRACT: Inkjet printing offers a low-cost, high-throughput avenue for producing functional organic materials through rapid translation of desktop discoveries to industrial roll-to-roll processes. Here, we report a simple, but effective strategy to control droplet coalescence during inkjet printing, as a major variable, to tailor the nanoscale morphology of organic composite materials produced upon evaporation of all-liquid inks. During deposition, the spacing between ink droplets was controlled to systematically vary the extent of droplet coalescence. Our results show that decreasing coalescence increased the solvent evaporation rate, supersaturation of the solutes, and nucleation density of the precipitating organic crystals. This phenomenon was utilized to tailor the average size of pentaerythritol tetranitrate (PETN) crystals dispersed in an adhesive binder matrix from ~0.2 to upwards of 100 μm. The results suggest that controlling the extent of droplet coalescence can be used as an effective means to tailor the composite morphology of printed organic materials at the nanoscale.

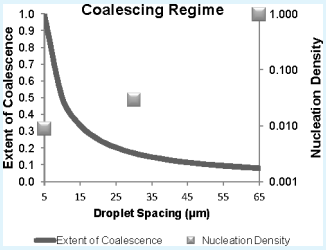

KEYWORDS: *inkjet printing, organic nanocomposite materials, droplet spacing, ink droplet coalescence, supersaturation, crystal nucleation and growth*

INTRODUCTION

The commercialization of piezoelectric-based drop-on-demand inkjet printers provides a low-cost, high-throughput avenue for integrating functional organic materials into flexible electronic devices through rapid translation of desktop discoveries to industrial roll-to-roll processes.[1−4] To date, numerous materials have been printed, from metals to ceramics to human cells.[5−8] This broad range of materials is evidence of: (1) the unique material processing capabilities of inkjet printing and (2) its application to an extensive range of industries. The appeal of printing technology is seen in the rate of published papers, increasing from less than 10 to about 600 publications per year from 1990 to 2010. To support this new technology, significant research efforts are being made to understand how ink formulation and processing factors influence the structure and properties of printed materials. Techniques have been described to exert control over deposition, or pattern, resolution in addition to methods for controlling the well studied radial and Marangoni flows which develop in evaporating ink to produce uniform material depositions.[9−14]

We recently demonstrated the ability to inkjet-print nanoscale organic composite materials for energetic and drug-elution applications.[15−18] For example, we prepared inkjet-printed micropatterns consisting of ~100 nm rifampicin (RFP) antibiotic crystals dispersed in a bioresorbable poly(D,L-lactic-*co*-glycolic) acid (PLGA) matrix. The micropatterns were found to be effective as infection-resistant surfaces, and through simple changes in ink formulation, it was possible to alter the functional nature of printed materials.[16] In another example, we reported the preparation of cyclotrimethylenetrinitramine (RDX) crystals dispersed in a cellulose acetate butyrate (CAB) matrix by direct-phase transformation from organic solvent-based all-liquid inks, with the RDX crystal size ranging from ~300 nm to 1 mm. We found that the evaporation rate of the ink, in combination with the microfluidic ink droplet confinement of the growing phases, were the key variables which determined morphology development in the inkjet-printed composites. Smaller organic crystals were produced with faster evaporation and increased microfluidic confinement.[18] These results provided new insights as to how the nanocomposite morphology and functionality of inkjet-printed organic materials can be tailored by controlling ink formulations and printing parameters.

This "one-step, all-liquid" ink formulation and printing approach offers several advantages over suspension-based inks. It removes the need for an additional material processing step to produce printable nanomaterials, as well as their handling, as bulk materials are dissolved in the ink. This also helps prevent clogging of the print head nozzles and the need to use sonication or surfactants to maintain a stable suspension. Finally, the only material waste generated in the process is the solvent lost to evaporation.

The goal of this study was to investigate a novel control strategy to tailor the morphology of the organic crystal phase through systemic variations of ink droplet coalescence on the substrate. In high-speed multi-nozzle inkjet printing, the

Received: June 11, 2012
Accepted: August 22, 2012
Published: September 5, 2012

   dx.doi.org/10.1021/am301050n | *ACS Appl. Mater. Interfaces* 2012, 4, 4691−4699

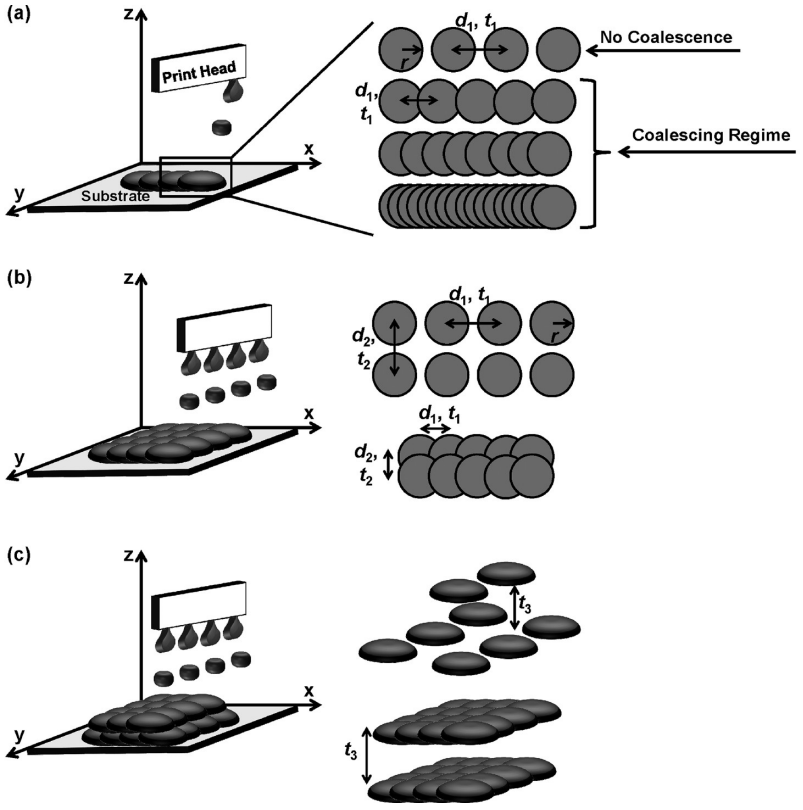

Figure 1. Multi-nozzle inkjet printing with droplet spacing (d_i) and time intervals (t_i) for: (a) a single row of droplets, (b) droplets in the *x*- and *y*-directions, and (c) droplets in the *x*-, *y*-, and *z*-directions.

evaporation and confinement variables can be correlated to ink droplet coalescence. Droplet coalescence occurs when neighboring droplets come into contact with each other, fusing together to form a continuous feature and larger pool of the ink droplets. This process is influenced by a number of factors, including surface chemistry interactions between substrate and droplet, environmental conditions, and droplet spacing.[19,20]

Ink droplet coalescence occurs within the coalescing regime, schematically illustrated in Figure 1a. The coalescing regime consists of the range of droplet spacing values from the minimum spacing distance, 5 μm for the printing platform used in this study, to the maximum distance at which two droplets will come into contact and fuse together to form a continuous feature. The maximum value is a function of the feature size of a droplet when deposited on the target substrate.

Droplet coalescence can occur in the *x*-direction, the *x*- and *y*-directions, and the *x*-, *y*-, and *z*-directions. Figure 1 is a schematic illustration of the potential directions of print (and coalescence) in multi-nozzle inkjet printing with the major droplet spacing and time intervals. During the ink deposition process, the print head moves in the positive *x*-direction while the substrate moves in the negative *y*-direction. This allows the possibility to print a single row of droplets in the *x*-direction using a single nozzle (Figure 1a) and droplets in the *x*- and *y*-directions (Figure 1b) and droplets in the *x*-, *y*-, and *z*-directions (Figure 1c) using multiple nozzles. The droplet spacing interval is the distance measured on-center between adjacent droplets and can occur in the *x*- and *y*-directions, expressed as d_1 and d_2, respectively, and described in Figure 1a,b. When printing large features with multiple nozzles, d_1 and d_2 typically have equivalent values. There is no droplet spacing interval in the *z*-direction, as additional layers are deposited on top of previously printed material and these droplets will have d_1 and d_2 spacings equivalent to previous layers. The ink droplet spacing was used to control droplet coalescence.

In this study, ink droplet coalescence was used as the key variable to control the morphology of organic/polymer composites containing: (1) pentaerythritol tetranitrate, commonly known as PETN, as a model organic crystal and (2) either polyvinyl acetate (PVAc) or chlorinated paraffin wax as model binder or adhesive materials. Here, we report that: (1) decreasing the extent of droplet coalescence results in faster solvent evaporation, increased supersaturation of the solutes, and increased nucleation density of the precipitating organic crystals and (2) the composite morphology of an inkjet-printed material can be tailored by controlling ink droplet coalescence. The printing process was separated into *x*-, *y*-, and *z*-directions, and the mechanisms which affect morphology development of the organic crystal phase in each direction were identified. The broad length scale over which composites were printed demonstrates the unique capabilities of inkjet printing as a transformational processing technique to produce nanoscale tailored composite materials while minimizing material use, handling, and waste generation.

EXPERIMENTAL METHODS

Ink Formulation. A previously described one-step, all-liquid ink formulation approach was used.[17,18] Briefly, PETN powder (provided by U.S. Army-ARDEC) and a binder material were dissolved in ethyl acetate (≥99.5%, Sigma-Aldrich, St. Louis, MO; solubility ~106 g PETN/kg solvent at ~20 °C;[21] PETN/binder ratio ~9:1). Two different binder materials were used, poly(vinyl acetate) (PVAc, M_w = 113 000, Sigma-Aldrich, St. Louis, MO) and a chlorinated wax (Chlorez 700S, Dover Chemical Corporation, Dover, OH). A piezoelectric drop-on-demand Dimatix DMP-2800 materials printer

(Fujifilm Dimatix, Santa Clara, CA) was used to print the inks. Cartridges which produced 10 pL ink droplets were used for this study. The inks were passed through a 0.2 μm nylon filter (Fisher Scientific, Pittsburgh, PA) to remove large, undissolved materials or contaminants which may have unintentionally entered the ink prior to printing.

Substrate Preparation. (100) silicon wafers with one side polished were used as substrates. After rinsing with deionized water (resistance 18.2 MΩ, Millipore, Bedford, MA), the substrates were placed polished surface up in a glass container and cleaned using a piranha solution. *Caution: dangerous solution, handle with care!* Sulfuric acid (H_2SO_4, 95−98%, Sigma-Aldrich, St. Louis, MO) and hydrogen peroxide (H_2O_2, 35 wt %, Sigma-Aldrich, St. Louis, MO) were added to the container (3:2 ratio) to sufficiently cover the substrates. After sitting for 1 h, the substrates were removed and thoroughly rinsed with and stored in deionized water until use. The substrates were dried in air prior to sample generation.

Sample Generation. Using the PETN−PVAc ink, a single row of droplets was deposited on the silicon substrates to study the effect of droplet coalescence in the *x*-direction on morphology development by varying d_1 during printing. A simple line feature was printed using one nozzle to deposit the single row of droplets with the print head moving in the positive *x*-direction across the stationary substrate. To look at several coalescing conditions, the spacing between the ink droplets was varied at 5, 30, and 65 μm, corresponding to maximum, intermediate, and minimum coalescing conditions, respectively. The intermediate value of 30 μm was chosen as a midpoint between the smallest droplet spacing for the printer used, 5 μm, and 65 μm, which was the largest spacing at which droplets still overlapped and formed a continuous feature. The substrate temperature and cartridge height were kept constant. Following this, using both the PETN−PVAc and PETN−wax inks, samples were generated to study the effect of droplet coalescence in the *x*- and *y*-directions and the *x*-, *y*-, and *z*-directions on morphology development by varying d_1 and d_2 during printing while depositing single and multiple layers of droplets. This was conducted to observe (1) morphology development in multidimensional features and (2) if altering the binder material caused any major changes in morphology development trends in printed composites. The extremes of maximum coalescence-like and no coalescence-like conditions were investigated. For the former condition, d_1 and d_2 were set at 5 μm and single (*x*- and *y*-directions) and multilayer (*x*-, *y*-, and *z*-directions) samples were generated. For the latter conditions, d_1 and d_2 were set at 100 μm. Under this setting, a single layer (*x*- and *y*-directions) sample contained an array of single droplet features. To prevent the formation of a pillar-like array on the substrate when printing the multilayer (*x*-, *y*-, and *z*-directions) sample, the substrate was shifted so subsequent depositions fell between previously printed features, thus forming a continuous feature. The substrate was shifted again for each subsequent deposition. The time between subsequent layer depositions, t_3, was adjusted in multilayer samples to ensure that the previously deposited ink had evaporated prior to depositing subsequent layers. Under both conditions, the samples had lateral dimensions of several millimeters. The substrate temperature and cartridge height were kept constant.

Characterization. Printed samples were characterized with dual-beam microscopy (SEM, Auriga FIB-SEM workstation, Carl Zeiss Microscopy, Peabody, MA). The samples were imaged "as-printed" with 1.0 kV of primary electron beam energy to prevent significant beam radiation damage to the PETN phase. The secondary electron (SE) signal was typically used for imaging the sample surface as it provided good image contrast and a significantly better portrayal of the surface morphology. A working distance of ∼4 to 5 mm was used. Cross-section views of select samples were also imaged in the FIB-SEM using a 30 kV focused ion beam (FIB) milling technique under cryogenic conditions to minimize ion beam damage to the sample during the mill.[22] Prior to cooling the sample for FIB-milling, a gold−palladium coating was sputtered (Structure Probe, Inc., West Chester, PA) onto the sample surface to reduce sample charging. The sample was cooled to −135 °C and maintained at that temperature during FIB-milling and microscopic characterization (VCT-100, Leica Microsystems, Inc., Buffalo Grove, IL). Prior to milling, an additional platinum coating (typically ∼1 μm) was deposited on the surface inside the FIB-SEM using a gas injection system to further minimize damage to the sample.[22] FIB-milling was then used to create the cross-section surface for imaging and was conducted at several locations on the sample. At each location, a series of images was captured as the sample was milled.

RESULTS

Ink Formulation, Jetting, and Single Droplet Depositions. During initial formulation, various solvents were investigated before settling on ethyl acetate. The solvent was jetted through significant adjustment to the waveform, which converts electric power to kinetic energy in the piezoelectric print head when ejecting a droplet. The waveform parameters were determined through iterative testing of the ejection, dampening, and standby segments in conjunction with firing voltage adjustments to develop a combination which produced consistent ink droplets.

Following successful jetting of pure ethyl acetate, the PETN and binder materials were dissolved in the solvent. The dissolved compounds did not significantly alter the ink's properties, and typically, only small adjustments to the firing voltage were needed to successfully jet the inks, with an example shown in Figure 2a. This (inverted) image was captured from a camera built into the printer. The camera was used to visualize the effects of the jetting parameter adjustments (waveform, firing voltage, etc.) on the velocity and shape of ejected droplets. Prior to each deposition, a short "purge" (using pressure to push ink out of the print head) procedure was used to clean the print head. For the size of the patterns printed, no cleaning was required mid-deposition as nozzle clogging was not encountered. Further work is necessary to develop a best practice cleaning procedure which minimizes material waste while keeping the print head functional for a given ink and pattern.

The typical composite morphology of single droplet depositions of PETN−PVAc and PETN−wax composites on silicon are shown in Figure 2b,c, respectively. The PETN−PVAc composite, Figure 2b, had a coffee ring structure typical of inkjet-printed materials. The PETN crystals ranged from about 200 to 500 nm in size and had a round island morphology. The PETN islands were more densely populated around the perimeter of the feature. The phase distinction was based on the sensitivity of the PETN phase to electron beam damage during scanning electron microscopy (SEM) characterization. The PETN−wax composite, Figure 2c, had a substantially different morphology, with the majority of material located in the center of the deposition. It was not possible to identify individual crystals in Figure 2c. It is important to note that the features shown in Figure 2b,c are representative of the composite morphology of the initial, single layer of droplets deposited when producing no coalescence-like samples while printing in the *x*-, *y*-, and *z*-directions, discussed below.

Morphology Development in a Line Feature. Figures 3 and 4 illustrate the effect of droplet coalescence in the *x*-direction, due to changes in d_1 in a line feature, on morphology development of printed PETN−PVAc materials on a silicon substrate. Figure 3a,b,c shows the effect of droplet coalescence on morphology development for maximum, intermediate, and minimum coalescing conditions produced using a d_1 of 5, 30, and 65 μm, respectively. Schematic insets (not to scale) in

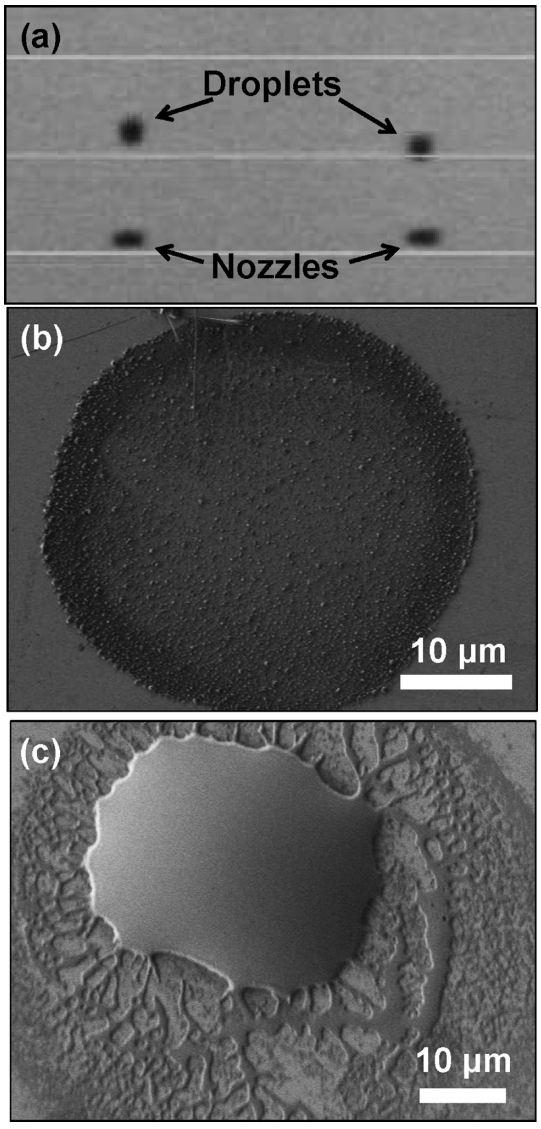

Figure 2. (a) All-liquid ethyl acetate-based 10 pL ink droplets jetting from cartridge nozzles. (b and c) Morphology of single droplet depositions of PETN−PVAc and PETN−wax composites, respectively, on silicon.

Figure 3 illustrate relative changes in droplet spacing for each of the samples as well as the *x*-direction of print for each image. In all images, the PVAc binder phase was the dark, amorphous shaped features while the PETN phase varied in morphology. The phase differentiation was based on: (1) the previously documented morphologies of PETN[23−26] and (2) the sensitivity of the PETN phase to electron beam damage during SEM characterization.

In Figure 3a,b, the edges of the line feature remain relatively parallel throughout the printed pattern and display the macroscale structure typical of coffee ring phenomena, though it was slightly less prominent in Figure 3b. The lines were ∼190 and ∼110 μm in width for Figure 3a,b, respectively, indicating that the droplets formed a large pool on the substrate after coalescing. In Figure 3c, the edges of the feature began to undulate or form a scalloped pattern. There was also evidence of satellite droplets (highlighted with arrows) being deposited; however, they had no impact on the morphology of materials within the deposition. At the widest point, the printed feature is ∼55 μm in width (excluding the satellite droplet) and about 10−20 μm at the narrowest point where successive droplets came into contact.

In Figure 4a, under maximum coalescing conditions (d_1 = 5 μm), the PETN phase had three distinct morphological structures. In the interior of the printed feature, the crystals formed both dendrite and long island structures. These structures were approximately 700 nm to 1 μm in width and ranged from about 2 to 10 μm in length. The PETN also formed a composite structure with the PVAc binder. Here, it appeared that the PETN crystals protruding from the PVAc were again approximately 700 nm to 1 μm in width and dispersed throughout the binder matrix. This morphology was prevalent along the edges of the feature, as well as in the large PVAc islands scattered within the interior.

Under intermediate coalescing conditions (d_1 = 30 μm), Figure 4b, the PETN phase tended to not form dendrites. Rather, the morphology consisted principally of both round island and needle-like structures, as well as the composite structure with the PVAc phase. The PETN island structures were slightly smaller than those in Figure 4a. Here, the round islands were approximately 500 nm to 1 μm in size while the needle-like structures were 500 nm to 1 μm wide and ranged from about 2 to 8 μm in length. The composite structure was again prevalent along the edges of the printed feature and in the PVAc islands scattered throughout the interior. The morphology of the PETN in the composite structure was similar to that in Figure 4a, with protruding crystals approximately 700 nm to 1 μm in width and dispersed throughout the matrix.

Under minimum coalescing conditions (d_1 = 65 μm), Figure 4c, there was no evidence of large PETN structures. Here, the crystals had a small, round island morphology ∼200−300 nm in diameter. They also appeared to be slightly more densely populated near the edges of the deposition. It was not possible to determine whether the PVAc islands formed a composite structure as above, due to the difficulty in resolving any individual PETN crystals within the structure.

Multidimensional Features and Different Binders. Figures 5 and 6 show the effect of droplet coalescence in the *x*- and *y*-directions (single layer) and *x*-, *y*-, and *z*-directions (multilayer) due to changes in d_1 and d_2 in a larger, rectangle feature on morphology development of printed composites. Figure 5 shows the surface morphology of PETN−PVAc samples printed on silicon. Figure 5a illustrates the surface morphology of samples printed under a maximum coalescence-like condition with $d_{1,2}$ set at 5 μm and a single layer of droplets deposited. The PETN crystals ranged from about 15 to 100 μm in length and between 5 and 10 μm in width and were typically square, rectangular, or leaf-like in shape and grew from perpendicular to parallel orientations to the substrate.

Figure 5b illustrates the surface morphology of multilayer samples printed under a minimum coalescence-like condition with $d_{1,2}$ set at 100 μm and a t_3 of about 10 seconds. From a macroscale perspective, the surface in Figure 5b was characterized by circular and granular features. The circular features on the surface were typically up to about 50 μm in diameter, and there was also evidence of coffee ring development occurring in this "top layer." This phenomenon appeared to occur when a droplet was deposited on previously printed material. The granular features did not appear to be distinct from the rest of the surface in the manner that particulate matter would settle onto a surface. It is speculated that these are the result of droplets (or satellite droplets) which

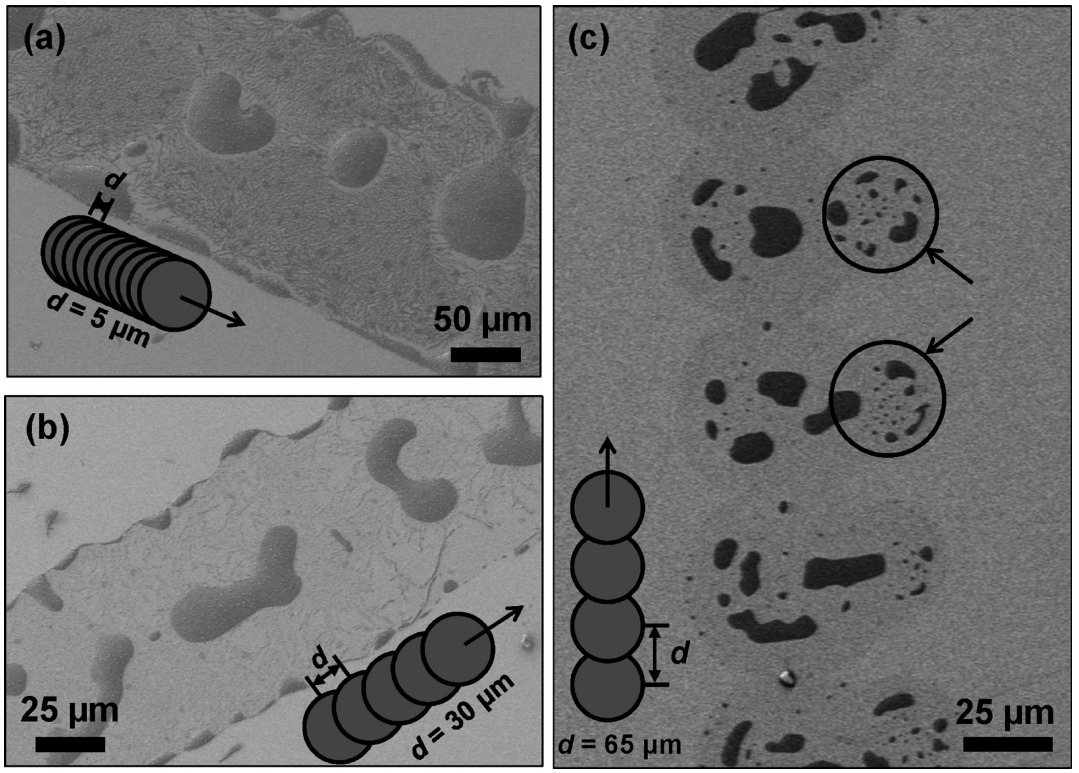

Figure 3. Morphology variation of PETN−PVAc composite on silicon in a line feature within the coalescing regime with d_1 set at: (a) 5, (b) 30, and (c) 65 μm. Schematic insets (not to scale) describe print x-direction in the images and relative changes in droplet spacing between samples.

partially aerosolized between the print head and the substrate and are typically ∼10 μm in diameter.

Figure 5c,d illustrates the two morphological structures highlighted in Figure 5b. Figure 5c shows the morphology typical of areas not characterized by a coffee ring structure (such as those labeled "c" in Figure 5b). Here, the printed material consisted of a somewhat porous structure which resembled an agglomeration of powder-like granules less than 1 μm in size. In contrast, Figure 5d shows larger PETN crystals typically 2−5 μm in length and about 500 nm to 1 μm in width, which was characteristic of the morphology in the coffee ring regions (those labeled "d" in Figure 5b).

Figure 6 depicts the surface and cross-section morphology of PETN−wax samples on silicon. Figure 6a illustrates the surface morphology of samples printed under a maximum coalescence-like condition with $d_{1,2}$ set at 5 μm and a single layer of droplets deposited. Here, the PETN crystals ranged from about 25 to 125 μm in length and were typically between 10 and 20 μm in width. The crystals were again square, rectangular, or leaf-like in shape in random orientations to the substrate. Figure 6b illustrates the cross-section morphology of samples printed with $d_{1,2}$ set at 5 μm and multiple layers of droplets deposited with t_3 about 10 seconds. The cross-section was produced by fracturing the sample after printing. The cross-section suggested the sample consisted of large, randomly oriented PETN crystals throughout the deposition. This interpretation was based on (1) the absence of distinct layers through the depth of the structure and (2) the inability to identify numerous crystals. The surface morphology of this sample, visible on the right hand side as viewing Figure 6b, consisted of large rectangular crystals.

Figure 6c illustrates the surface morphology of multilayer samples printed under a minimum coalescence-like condition with $d_{1,2}$ set at 100 μm and t_3 about 10 seconds. The surface was again characterized by circular and granular features. While the granular features were similar to those described in Figure 5b and ∼10 μm in size, the circular features were somewhat smaller, typically 35−40 μm in diameter. They again appeared to sit "on top" of previously printed material. It was difficult to identify any individual PETN crystals from the surface morphology, highlighted with higher magnification in Figure 6d. Note that Figure 6d was captured with the SEM stage at 54°.

Figure 6e,f shows a cross-section image of the multilayer PETN−wax composite printed under a no coalescence-like condition. Figure 6f was captured using the microscope's ESB detector (backscattered electrons). Figure 6e suggests the morphology was a nanocomposite structure consisting of about 200−300 nm PETN crystals dispersed in a discrete and continuous binder matrix. Within the printed composite, the wax phase has the light contrast while the PETN phase has the darker contrast. This phase differentiation was determined by: (1) an enhanced contrast difference seen using the ESB detector as well as the (2) sensitivity to beam damage of the darker phase which was expected even when cooled after prolonged beam exposure. This contrast and damage is clearly visible when comparing Figure 6e,f, where the dark phase has an increased amount of beam damage in Figure 6f (example highlighted with arrow) relative to Figure 6e. During characterization, there was also evidence of voids throughout the structure, in some cases several micrometers in size.

DISCUSSION

The development of radial flow in evaporating droplets has been well studied. This phenomenon produces a coffee ring structure which has been well documented in inkjet-printed

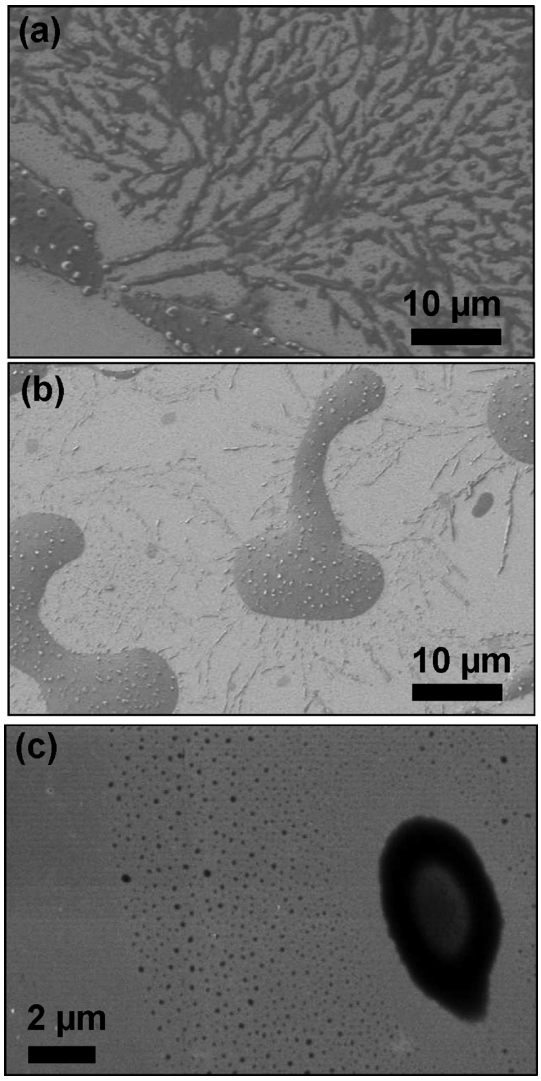

Figure 4. PETN morphology variation in a line feature within the coalescing regime with d_1 set at: (a) 5, (b) 30, and (c) 65 μm.

materials, due to a flux of fluid toward the pinned edge of the deposition and a buildup of solute or suspended particulates around the edge as the ink evaporates.[10,27] The large crystals seen in the coffee ring structures in Figure 5b,d were likely the result of an increase in contact line pinning due to droplets being deposited on a rough or topographic material surface (as opposed to the polished silicon wafer). Previous work has shown that surface topographies influence contact line pinning in an evaporating droplet.[28] We speculate that an increase in contact line pinning (and thus radial flow) occurred, causing solute to be transported to the edges of the evaporating droplet where crystal nucleation and growth occurred, resulting in the formation of larger crystals in the "top layer." We were unable to definitively determine whether the lack of a similar structure in Figure 6c,d was the result of a competing Marangoni flow[11,29] and/or material–ink interactions causing a de-pinning of the contact line.

The results show that by varying the extent of ink droplet coalescence it was possible to produce composite materials with diverse crystal morphologies. When printing in the *x*-direction and *x*- and *y*-directions, the changes in morphological structure development in printed materials appear to be the result of (1) variations in the evaporation of the solvent-based ink and (2) corresponding changes in volume and solute concentration. When printing in the *z*-direction, morphology development during multilayer printing appears to be due to either (1) continuous- or (2) re-nucleation of printed material.

We postulate that the effect of droplet coalescence in the *x*-direction and *x*- and *y*-directions on PETN crystal size can be explained using classical nucleation theory. Crystal nucleation begins to occur once a critical supersaturation is obtained in the solution.[30] The rate (J) at which this occurs can be described as:[31]

$$J = AS \exp\left(\frac{-B}{\ln^2 S}\right) \quad (1)$$

where A is the diffusion-limited rate of nucleation, B is the thermodynamic parameter, and S is the supersaturation which is a ratio of the solute concentration to its solubility in the solution.

In this study, the inks were not formulated with the solute at the critical supersaturation and ink evaporation occurred rapidly. Therefore, ink evaporation is the mechanism which increases supersaturation within the printed ink leading to crystal nucleation. The evaporation rate of the ink after being deposited on the substrate is influenced by factors such as droplet (or deposition) size, substrate and atmosphere temperature, atmosphere vapor content, and gas convection across the deposition, among others, that control the diffusion of vapor away from the liquid–vapor interface.[32,33] As all samples were printed under similar conditions, changes in the evaporation rate of deposited ink were likely due to variations in deposition size or the amount of ink pooling on the substrate, corresponding to the extent of ink droplet coalescence.

The influence of size on evaporation rate has been illustrated in a single droplet system, where the evaporation rate changes with droplet radius.[32,33] The evaporation rate of a droplet will decrease with an increase in radius. Previous work studying printed feature shapes has shown that changing the ink droplet spacing in a line will influence the uniformity, shape, and size of a deposition.[19,20] Our results showed similar behavior and that changing the droplet spacing significantly altered the size of a deposition and degree of ink pooling on the substrate, as illustrated in Figure 3.

Under our postulation, a large d_1 spacing will minimize deposition size and ink pooling, producing a faster ink evaporation rate and leading to a more rapid increase in the concentration of dissolved materials, a higher supersaturation (S) within the printed ink, and a higher nucleation rate (J). Figure 7 summarizes the relationship between d_1, the extent of droplet coalescence, and the nucleation density of the PETN phase. The extent of droplet coalescence is expressed as a dimensionless number, which is a slight modification of the volume of ink deposited per unit length described by Soltman and Subramanian.[19] The extent of droplet coalescence is defined as the ratio of the number of droplets deposited to produce a printed feature, a function of the droplet spacing, relative to the maximum number of droplets it would be possible to deposit using a droplet spacing of 5 μm:

$$\text{extent of coalescence} = \frac{\text{number of droplets deposited}}{\text{maximum number with 5 } \mu\text{m spacing}} \quad (2)$$

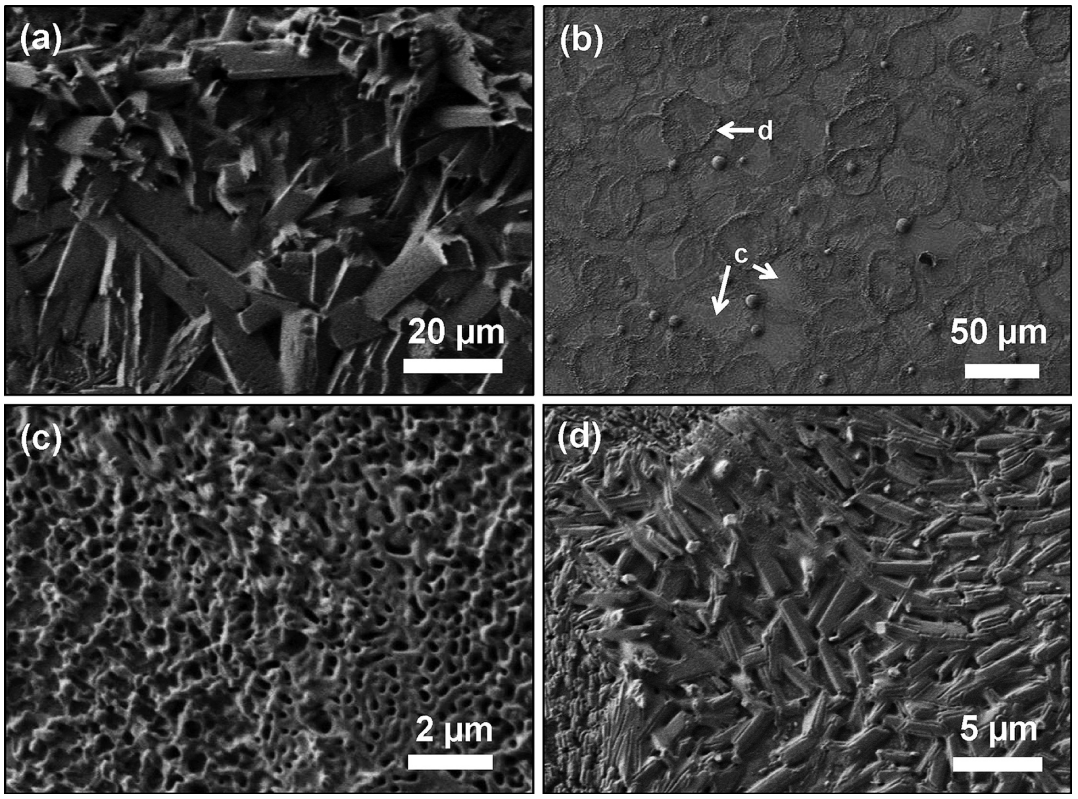

Figure 5. PETN−PVAc composite samples on silicon. (a) Surface morphology of a single layer deposition printed under maximum coalescence-like conditions using a $d_{1,2}$ of 5 μm. (b) Surface morphology of a multilayer deposition printed under minimum coalescence-like conditions using a $d_{1,2}$ of 100 μm. (c and d) Higher magnification images of characteristic morphology in areas labeled "c" and "d," respectively, in (b).

This relationship is only valid within the coalescing regime. An inverse relationship, a value of 1 corresponds to maximum coalescence which is produced using a minimum droplet spacing.

Evident in Figure 7, as the extent of droplet coalescence decreased, there was an exponential increase in the experimentally measured nucleation density of the PETN phase, as evident by the logarithmic secondary axis to the right of the graph. The plotted values are the normalized averages of the number of PETN crystals counted within three SEM images representative of the printed feature, similar to those shown in Figure 4. The standard deviations for maximum, intermediate, and minimum coalescing conditions are 0.02, 0.02, and 0.61, respectively. This increase in nucleation density corresponds with a reduction in PETN crystal size, as the phase is rapidly depleted by the large number of nuclei within the deposition resulting from a high supersaturation. Clearly visible in Figure 4, the crystal size decreased from up to 10 μm to ~200−300 nm in length as d_1 was increased from 5 to 65 μm.

The correlation between the extent of coalescence, supersaturation, and crystal size also appears to be operative during multidimensional printing. By preventing droplet coalescence in the *x*- and *y*-directions with a large $d_{1,2}$ spacing, the ink evaporated rapidly, causing a high supersaturation within the printed ink. As a result, the growth of the PETN phase was arrested in the nanoscale, illustrated in Figure 2b where PETN crystals were 200−500 nm in size and in Figure 2c where individual crystals were not identified, suggesting a nanocomposite structure. Conversely, when droplet coalescence was maximized with a small $d_{1,2}$ spacing, the ink evaporated relatively slowly. This resulted in a lower supersaturation within the ink and the growth of PETN crystals an order of magnitude larger in size, as illustrated in Figures 5a and 6a.

When printing multiple layers in the *x*-, *y*-, and *z*-directions, the morphology development in the *z*-direction appeared to be the result of either continuous- or re-nucleation of the organic crystal phase, schematically illustrated in Figure 8. When a small $d_{1,2}$ spacing was used, ink droplets coalesced to form a pool of ink on previously deposited material, described in Figure 8a. This high extent of coalescence correlated to a relatively slow evaporation and low supersaturation within the printed ink. In such a situation, morphology development was likely dominated by solute from subsequent layer depositions continuously nucleating and growing on existing PETN crystals. As suggested in Figure 6b, continuous-nucleation resulted in large crystals throughout the depth of the structure. Conversely, when a large $d_{1,2}$ spacing was used, ink droplets were prevented from coalescing, described in Figure 8b. The low extent of coalescence in subsequent depositions correlated to rapid ink evaporation and a high supersaturation of the solutes within the printed ink, resulting in re-nucleation of the organic crystal phase with each deposition. As suggested in Figure 6e,f, re-nucleation resulted in a nanocomposite structure through the depth of printed material.

A number of industries would potentially benefit from the ability to easily tailor the morphology of printed materials. Organic materials are used in applications ranging from biomedical and pharmaceutical to solar cells and electronics.[34−37] Controlling the size, shape, and structure of materials is essential for producing desired properties. For example, it has been documented how the morphology and composition of pharmaceutical particles will affect their

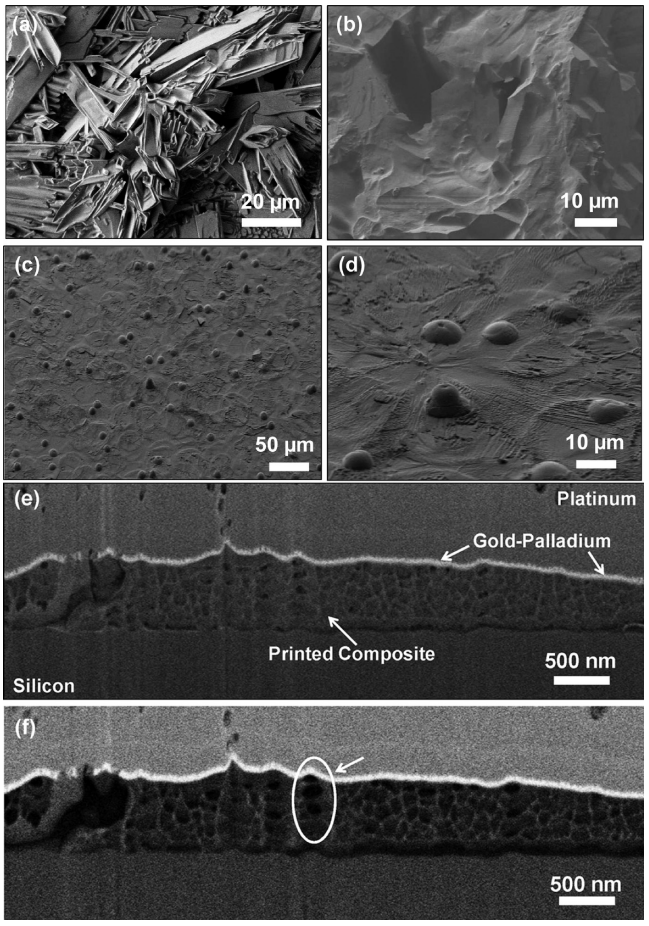

Figure 6. PETN–wax composite samples printed on silicon. (a) Surface morphology of a single layer deposition printed under maximum coalescence-like conditions using a $d_{1,2}$ of 5 μm. (b) Cross-section of multilayer maximum coalescence-like sample. (c) Surface morphology of a multilayer deposition printed under minimum coalescence-like conditions using a $d_{1,2}$ of 100 μm with (d) higher magnification. (e and f) Select cross-section of FIB-milled multilayer sample printed under minimum coalescence-like conditions. (f) Image captured using ESB detector.

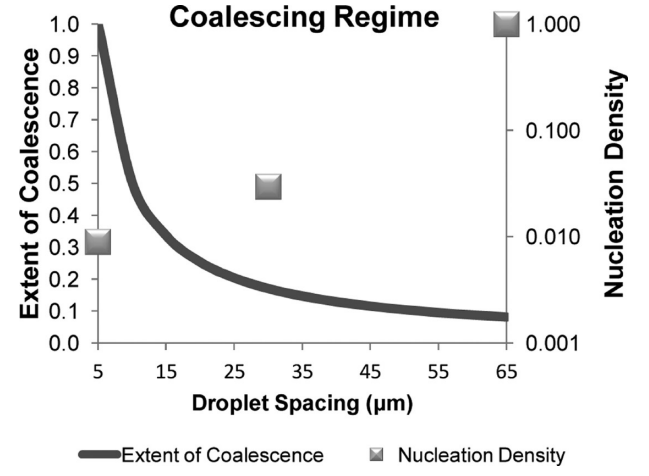

Figure 7. Correlation between d_1, the extent of droplet coalescence, and nucleation density of the PETN phase in a line feature within the coalescing regime.

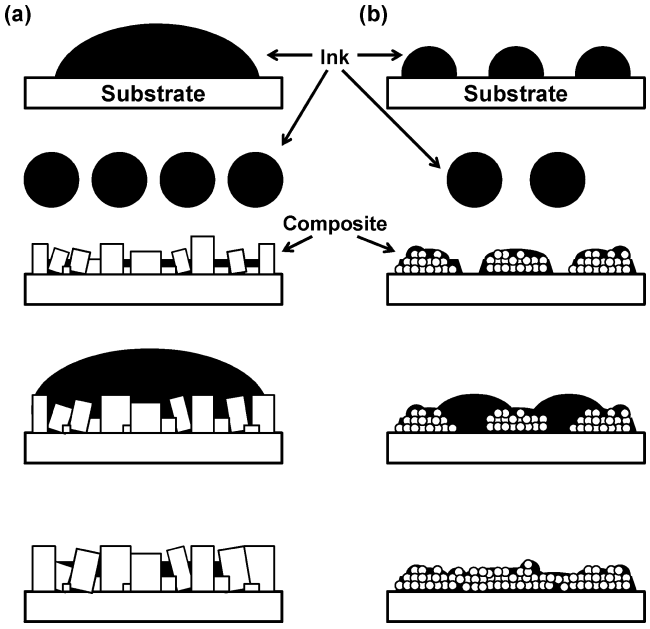

Figure 8. Schematic illustrations of (a) continuous-nucleation and (b) re-nucleation of the organic crystal phase under maximum and minimum coalescence-like conditions, respectively, when printing multiple layers in the *z*-direction.

bioavailability through changes in the initial burst and steady-state release rate.[34] In a similar respect, the performance of organic-based bulk heterojunction solar cells is influenced by, among other aspects, the nanoscale morphology of the materials contained in the photoactive layer.[36] Further, a composite material's mechanical properties are influenced by factors such as morphology and composition.[38−40]

The ability to deposit organic composites over a variety of length scales demonstrates the potential of the one-step, all-liquid ink formulation approach as a low-cost, high-throughput method for material synthesis. It has been shown that, by controlling the extent of droplet coalescence, it was possible to produce composite materials with the organic crystal phase ranging from 100's of nanometers to 10's of micrometers in size. In addition, this material synthesis route also offers several advantages from a process perspective, as the direct-phase transformation of liquid inks to micro- and nanocomposite structures minimizes material use, handling, and waste generation.

CONCLUSIONS

Organic composite materials were produced over a broad length scale by the direct-phase transformation of all-liquid ink to composite material. Composite characterization indicated that variations in the extent of ink droplet coalescence during printing generated diverse material morphologies. When printing in the *x*-direction and *x*- and *y*-directions, variations in organic crystal morphology correlated to changes in the supersaturation within the ink as it evaporated, which was strongly influenced by the extent of ink droplet coalescence due to changes in the d_1 and d_2 spacing. Decreasing the extent of droplet coalescence reduced the PETN crystal size from about 10 μm to ~200–300 nm in a line feature and from upwards of 100 μm to ~200–500 nm in a rectangular feature. In the *z*-direction, the three dimensional structure development was the result of either continuous- or re-nucleation of the organic

crystal phase, which was also influenced by the supersaturation of ink in subsequent depositions. Depending on the relative supersaturation, crystals either continuously nucleated and grew on previously deposited material or re-nucleated with each deposition, resulting in a structure composed of micro- or nanoscale PETN crystals, respectively. The results suggest that by controlling the extent of ink droplet coalescence during printing it is possible to vary the evaporation rate and supersaturation of the solute as the ink evaporates, as a novel strategy to tailor the nanoscale morphological structure of printed materials.

AUTHOR INFORMATION

Corresponding Author

*Address: Chemical Engineering and Materials Science, Stevens Institute of Technology, Castle Point on Hudson, Hoboken, NJ 07030 USA. Phone: 1-201-216-8307. Fax: 1-201-216-8306. E-mail: wlee@stevens.edu.

Author Contributions

The manuscript was written through contributions of all authors. All authors have given approval to the final version of the manuscript.

Notes

The authors declare no competing financial interest.

ACKNOWLEDGMENTS

We thank Professor Chang-Hwan Choi and Mr. Wei Xu of Stevens for their thoughtful discussions about droplet evaporation. We also thank Dr. Daniel Stec III of SAIC and Mr. Rodger E. Cornell of U.S. Army-ARDEC for laboratory support. This research was sponsored by the U.S. Army under contract W15QKN-05-D-0011 and used SEM-FIB microscope resources partially funded by the National Science Foundation through NSF Grant DMR-0922522.

REFERENCES

(1) Hon, K. K. B.; Li, L.; Hutchings, I. M. *CIRP Ann. Man. Tech.* **2008**, *57*, 601−620.
(2) Pique, A.; Chrisey, D. B.; Eds. In *Direct-Write Technologies for Rapid Prototyping Applications: Sensors, Electronics, and Integrated Power Sources*; Academic Press: San Diego, 2002; p 15−16.
(3) Calvert, P. *Chem. Mater.* **2001**, *13*, 3299−3305.
(4) Basiricò, L.; Cosseddu, P.; Fraboni, B.; Bonfiglio, A. *Thin Solid Films* **2011**, *520*, 1291−1294.
(5) de Gans, B. J.; Duineveld, P. C.; Schubert, U. S. *Adv. Mater.* **2004**, *16*, 203−213.
(6) Singh, M.; Haverinen, H. M.; Dhagat, P.; Jabbour, G. E. *Adv. Mater.* **2010**, *22*, 673−685.
(7) Cappi, B.; Ozkol, E; Ebert, J.; Telle, R. *J. Eur. Ceram. Soc.* **2008**, *28*, 2625−2628.
(8) Parsa, S.; Gupta, M.; Loizeau, F.; Cheung, K. C. *Biofab* **2010**, *2*, 025003.
(9) Derby, B. *Annu. Rev. Mater. Res.* **2010**, *40*, 395−414.
(10) Deegan, R. D.; Bakajin, O.; Dupont, T. F.; Huber, G.; Nagel, S. R.; Witten, T. A. *Nature* **1997**, *389*, 827−829.
(11) Hu, H.; Larson, R. G. *J. Phys. Chem. B* **2006**, *110*, 7090−7094.
(12) Park, J.; Moon, J. *Langmuir* **2006**, *22*, 3506−3513.
(13) Yunker, P.; Still, T.; Lohr, M. A.; Yodh, A. G. *Nature* **2011**, *476*, 308−311.
(14) Shen, X.; Ho, C. M.; Wong, T. S. *J. Phys. Chem. B* **2010**, *114*, 5269−5274.
(15) Lee, J. H.; Gu, Y.; Wang, H.; Lee, W. Y. *Biomaterials* **2012**, *33*, 999−1006.
(16) Gu, Y.; Chen, X.; Lee, J. H.; Monteiro, D.; Wang, H.; Lee, W. Y. *Acta Biomater.* **2012**, *8*, 424−431.
(17) Ihnen, A. C.;; Fuchs, B.; Petrock, A.; Samuels, P.; Stepanov, V.; Di Stasio, A.; Lee, W. *Proceedings of the 14th International Detonation Symposium*, Couer d'Alene Resort, Idaho, April 11−16, 2010; pp 37−40.
(18) Ihnen, A. C.; Petrock, A. M.; Chou, T.; Samuels, P. J.; Fuchs, B. E.; Lee, W. Y. *App. Surf. Sci.* **2011**, *258*, 827−833.
(19) Soltman, D.; Subramanian, V. *Langmuir* **2008**, *24*, 2224−2231.
(20) Stringer, J.; Derby, B. *Langmuir* **2010**, *26*, 10365−10372.
(21) Roberts, R. N.; Dinegar, R. H. *J. Phys. Chem.* **1958**, *62*, 1009−1011.
(22) Stokes, D. J.; Hayles, M. F.; Phifer, D.; Findlay, K. C. *J. Microsc.* **2007**, *226*, 263−269.
(23) Tappan, A. S.; Knepper, R.; Wixom, R. R.; Miller, J. C.; Marquez, M. P.; Ball, J. P. *Proceedings of the 14th International Detonation Symposium*, Couer d'Alene Resort, Idaho, April 11−16, 2010; pp 1087−1095.
(24) Zhang, G.; Weeks, B. L. *App. Surf. Sci.* **2010**, *256*, 2363−2366.
(25) Zhang, G.; Weeks, B. L. *Scanning* **2008**, *30*, 228−231.
(26) Maiti, A.; Gee, R. H. *Propellants, Explos., Pyrotech.* **2009**, *34*, 489−497.
(27) Deegan, R. D.; Bakajin, O.; Dupont, T. F.; Huber, G.; Nagel, S. R.; Witten, T. A. *Phys. Rev. E* **2000**, *62*, 756−765.
(28) Kalinin, Y. V.; Berejnov, V.; Thorne, R. E. *Langmuir* **2009**, *25*, 5391−5397.
(29) Hu, H.; Larson, R. G. *Langmuir* **2005**, *21*, 3972−3980.
(30) Hurle, D. T. J., Ed. In *Handbook of Crystal Growth 1, Fundamentals Part A: Thermodynamics and Kinetics*; Elsevier: Amsterdam, 1993; p 251−306.
(31) He, G.; Bhamidi, V.; Tan, R. B. H.; Kenis, P. J. A.; Zukoski, C. F. *Cryst. Growth Des.* **2006**, *6*, 1175−1180.
(32) Berthier, J. In *Microdrops and Digital Microfluidics*; William Andrew: Norwich, NY, 2008; p 75−159.
(33) Hu, H.; Larson, R. G. *J. Phys. Chem. B* **2002**, *106*, 1334−1344.
(34) Hassan, A. S.; Sapin, A.; Lamprecht, A.; Emond, E.; El Ghazouani, F.; Maincent, P. *Eur. J. Pharm. Biopharm.* **2009**, *73*, 337−344.
(35) Monzon, M.; Oteiza, C.; Leiva, J.; Amorena, B. *J. Antimicrob. Chemother.* **2001**, *48*, 793−801.
(36) Moule, A. J.; Meerholz, K. *Adv. Funct. Mater.* **2009**, *19*, 3028−3036.
(37) Dimitrakopoulos, C. D.; Malenfant, P. R. L *Adv. Mater.* **2002**, *14*, 99−117.
(38) Fagundes, E. C. M.; Jacobi, M. A. M. *J. App. Polym. Sci.* **2012**, *123*, 3072−3080.
(39) Jordan, J.; Jacob, K. I.; Tannenbaum, R.; Sharaf, M. A.; Jasiuk, I. *Mater. Sci. Eng. A* **2005**, *393*, 1−11.
(40) Zhu, R.; Hoshi, T.; Chishima, Y.; Muroga, Y.; Hagiwara, T.; Yano, S.; Sawaguchi, T. *Macromolecules* **2011**, *44*, 6103−6112.